J Mater Sci (2009) 44:962–969
DOI 10.1007/s10853-008-3198-5

Investigation of early growth of calcium hydroxide crystals in cement solution by soft X-ray transmission microscopy

V. S. Harutyunyan · A. P. Kirchheim ·
P. J. M. Monteiro · A. P. Aivazyan ·
P. Fischer

Received: 5 July 2008 / Accepted: 15 December 2008 / Published online: 13 January 2009

Abstract The early growth of calcium hydroxide (CH) crystals in cement solution is investigated by soft X-ray transmission microscopy imaging. A quantitative analysis of the successively recorded images of the hydration process enabled to evaluate the supersaturation ratio of solution, growth rates, both kinetic and diffusion coefficients, and concentrations of solute molecules at $\{10\bar{1}0\}$ and $\{0001\}$ facets of the CH crystals. It is concluded that the difference in obtained concentrations of solute molecules at these facets may be associated with solubility anisotropy of crystallographic facets of the CH. The interfacial energy of the CH nuclei in aqueous solution is evaluated to be 0.114 J/m^2 that by an order of magnitude is smaller than the average free surface energy of this phase. The proposed theoretical approach is universal and, in potential, may be applied to any precipitating phase in a supersaturated solution.

Introduction

Research on cement hydration was performed at the full-field soft transmission X-ray microscope XM-1 located at beamline 6.1.2 at the Advanced Light Source (ALS), which is operated by the Center for X-ray Optics, Lawrence Berkeley National Laboratory, Berkeley, California. Previous research [1–3] has been conducted using this microscope for the in-situ observation and qualitative analysis of through-solution hydration products and products of topochemical reactions, which form in cementitious aqueous solutions. The high spatial resolution ($\approx$35 nm) of the microscope XM-1 provides a remarkable possibility to trace the *early* growth process of a precipitating individual particle in solution and to record both the size and shape variations in time. This may allow to investigate, at different physical conditions, the *dynamics* of the growth process and also to *grade* the growth rates of the main phases: calcium hydroxide (CH), ettringite, and calcium silicate hydrate that form in cementitious aqueous solution.

In this work, we focus our analysis on precipitation process in cement solution of the CH. The analysis of successive images of the hydration process provided critical quantitative information about the growth rate of CH crystals, the supersaturation ratio, the kinetic and diffusion coefficients, and some other important parameters characterizing the growth process.

Experiment

ASTM Type II Portland cement and 6% $C_4A_3\bar{S}$ admixture were mixed in aqueous solution saturated with respect to CH and gypsum. The overall goal of this research program was to study expansive cements, therefore, the $C_4A_3\bar{S}$ admixture was included in the experimental program because addition of $C_4A_3\bar{S}$ to Portland cement has been proven to generate ettringite and significant early-age expansion. For comparative analysis, second solution was

V. S. Harutyunyan (✉) · A. P. Aivazyan
Department of Solid State Physics, Yerevan State University, Yerevan, Armenia
e-mail: vharut@physic.ysu.am; vharut2003@yahoo.com

A. P. Kirchheim · P. J. M. Monteiro
Department of Civil and Environmental Engineering, University of California, Berkeley, CA, USA

P. Fischer
Center for X-ray Optics, Lawrence Berkeley National Laboratory, Berkeley, CA, USA

prepared by mixing 100% $C_4A_3\bar{S}$ admixture (i.e., no cement) in aqueous solution also saturated with respect to CH and gypsum. Both solutions were prepared with fresh, and boiled deionized water. For synchrotron radiation imaging, from both solutions the sample preparation procedure was the same. The solution/solid materials ratio was 10, which is higher than the ratio used in regular concrete and mortars; to compensate for this dilution, the solutions were originally saturated with CH and gypsum. The solid particles were mixed for 50 s in the solution, and then centrifuged for 15 s to remove large particles as the sample thickness is restricted to about 10 μm. After centrifugation procedure the solution/solid materials ratio decreased and was estimated to be 50. To allow sufficient transmission of the soft X-rays, a small droplet was taken from the supernatant solution and assembled in the sample holder, and then squeezed between two thin SiN windows for the analysis. Sample is viewed through these SiN windows which are sandwiched between stainless steel plates fitted with rubber *o*-rings to minimize evaporation and exposure to CO_2. The X-ray optical setup of the microscope XM-1 is described elsewhere [2]. This experiment used a wavelength of 2.4 nm (516.6 eV). The radiation transmitted by the sample was detected using an X-ray CCD camera, with a resolution of 35 nm and magnification factor of about 2000. The recorded images have a circular field of view of approximately 10 μm in diameter (see Figs. 1 and 2). The illumination time per image was in the range of 1–14 s.

For phase analysis of hydration products that form in 6% $C_4A_3\bar{S}$ admixture-containing solution, we recorded an X-ray diffraction (XRD) spectrum from a sample prepared from this solution. The sample has been prepared in the following way. Again, ASTM Type II Portland cement and 6% $C_4A_3\bar{S}$ admixture were mixed in aqueous solution saturated with respect to CH and gypsum. The solution/solid materials ratio was 50. After 2 h the solution was filtered rapidly for removal of water and the XRD spectrum has been recorded from remaining solids (see Fig. 3).

The experimental work was conducted at a room temperature $T = 298$ K.

Theoretical model and obtained results

Figure 1 shows X-ray images of the hydration process during the first 118 min immediately after the solution was prepared. The six images were recorded every 23.6 min, on average. On the basis of analysis of the soft X-ray images recorded from cementitious solutions by previous research [1–3], it may be concluded that the largest particle observable in the images presented in Fig. 1 is a Portland cement grain. In these images, it may be clearly traced that the precipitation of hydration products are both on and apart from the cement grain. The tiny fiber-like particles precipitating on the surface of the cement grains (see Fig. 1a–f) are thought to be a form of calcium silicate hydrate (C–S–H) or a form of silicate poisoned CH, a potential C–S–H precursor [1, 2]. Portland cement contains aluminate phases which in reaction with sulfate ions and water lead to the formation of ettringite crystals with hexagonal-prism shape. Using soft X-ray imaging technique, Juenger et al. [2] observed precipitation of large crystals, definitely belonging to ettringite, on the Portland cement grains in a dilute aqueous solution. Therefore, in Fig. 1b–f, the comparatively large particles precipitating on the cement grain and viewing with a cylinder-like shape presumably belong to ettringite (in Fig. 1f, these particles are indicated with white solid arrows). No formation of regularly-shaped crystals was observed during the first 15 min after the sample preparation (see Fig. 1a); it is assumed that this time-interval is associated with the nucleation period of the growing particles. The images presented in Fig. 1b–f, however, clearly show the growth process of crystals with a plate-like shape. These crystals are imaged in different crystallographic projections that definitely belong to particles with a hexagonal-prism shape, as is schematically depicted in Fig. 4. Previous research [4–7] has shown that the crystals of the CH precipitate with hexagonal-prism shape faceted by $\{10\bar{1}0\}$ prismatic and $\{0001\}$ basal facets, and exhibit aspect ratio r_L that satisfies the following condition:

$$r_L = L_1/L_2 \geq 1, \qquad (1)$$

where L_1 and L_2 are the characteristic linear sizes of a crystal, corresponding to $\langle 10\bar{1}0\rangle$ and $\langle 0001\rangle$ growth directions (see Fig. 4). Therefore, the regularly-shaped isolated particles observed in the recorded images in Fig. 1 were assumed to be the evidence of the CH phase, but not ettringite. Figure 2 presents the X-ray image recorded from the solution saturated with respect to CH and gypsum and containing 100% $C_4A_3\bar{S}$ admixture (i.e., no cement). The crystals seen in Fig. 2 are either ettringite or CH because of the chemistry of this solution. Formation of the CH could be expected due to evaporation of solution changing the system from CH-saturated to CH-supersaturated. However, this possibility is excluded since under experimental conditions of the applied technique any noticeable evaporation of water from the solution cannot take place during 2-h of experimental time. Besides, the needle-like shape of crystals in Fig. 2 is not typical of CH. As was demonstrated by Mehta [8] on the bases of scanning electron microscopy imaging and XRD analysis, 100% $C_4A_3\bar{S}$ admixture-containing solution is the most optimum condition for encouraging the formation of ettringite crystallites with prolonged hexagonal-prism shape. The indicated morphological peculiarity is typical of this phase and, as a rule, in

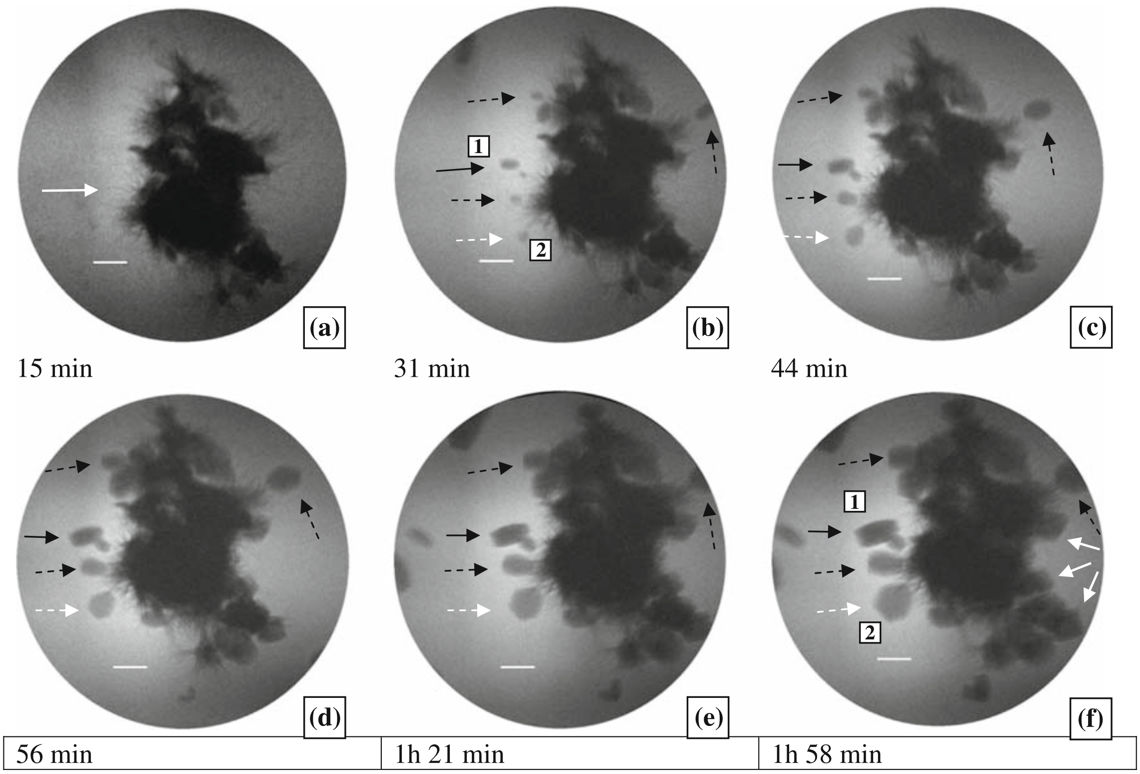

Fig. 1 Soft X-ray images of aqueous cement solution (ASTM Type II Portland cement and 6% $C_4A_3\bar{S}$ admixture; solution/solutes ratio was 50) saturated with respect to CH and gypsum. Images were recorded at a time-interval of 15–118 min immediately after solution preparation from a fixed volumetric region. Scale bar is 1 µm. White arrow in image (**a**) indicates a hydrating cement grain covered with tiny needle-like particles that are thought to be a form of calcium silicate hydrate (C–S–H) or a form of silicate poisoned CH, a potential C–S–H precursor. In images (**b**) to (**f**), solid arrows indicate the growth process of a CH crystal (numbered as particle No. 1), for which a quantitative analysis has been conducted in terms of growth parameters; dashed white arrows indicate a CH crystal (numbered as particle No. 2) with imaged {0001} basal facet, and dashed black arrows indicate another three growing crystals also identified as CH. In image (**f**), white solid arrows indicate the large crystals (presumably it is ettringite) that grow on the surface of the cement grain

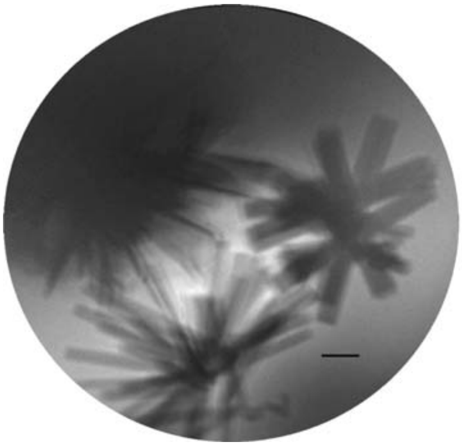

Fig. 2 Soft X-ray image of aqueous cement solution (100% $C_4A_3\bar{S}$ admixture; solution/admixture ratio was 50) saturated with respect to CH and gypsum. About 20 min of hydration. Scale bar is 1 µm

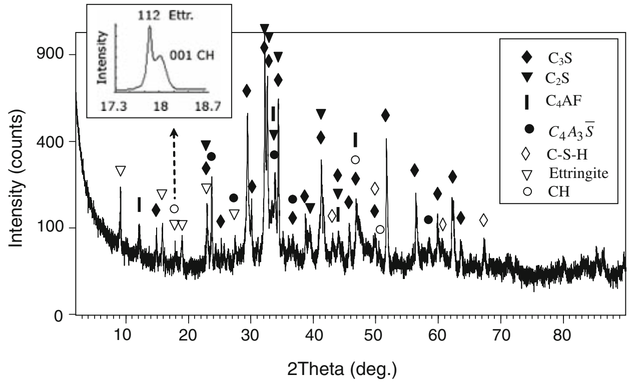

Fig. 3 XRD spectrum recorded from the sample prepared from ASTM Type II Portland cement and 6% $C_4A_3\bar{S}$ admixture-containing aqueous solution saturated with respect to CH and gypsum. The solution/solid materials ratio and hydration time of solution were 50 and 2 h, respectively. The inset shows the expanded view of the angular range that involves overlapping 112 ettringite ($2\theta = 17.8°$) and 001 CH ($2\theta = 18.1°$) diffraction peaks. The phase analysis was conducted according to the following JCPDS cards: No. 42-0551 for C_3S, No. 36-0642 and No. 33-0302 for C_2S, No. 30-0226 for C_4AF, No. 42-1478 for $C_4A_3\bar{S}$,No. 06-0010 and No. 06-0013 for C–S–H, No. 41-1451 for ettringite, and No. 04-0733 for CH

cemetitious materials, ettringite precipitates as needle-like crystallites with hexagonal-prism shape and aspect ratio $r_L = L_1/L_2 < 1$ (Fig. 4 depicts the growth facets also for an

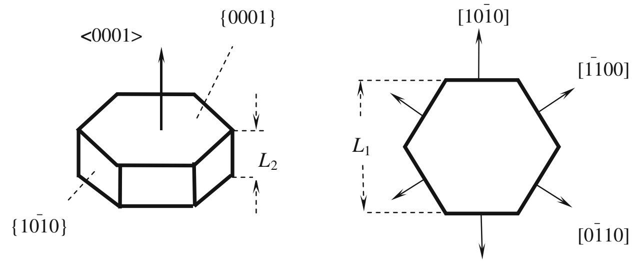

(a) **(b)**

Fig. 4 **a** Hexagonal-prism shape of a CH crystallite with {0001} basal and {10$\bar{1}$0} lateral facets. L_2 is the linear size along ⟨0001⟩ growth direction. **b** View at a {0001} facet. L_1 is the linear size of the crystallite in ⟨10$\bar{1}$0⟩ growth directions

ettringite crystallite). Clustering of precipitating crystallites is also typical of ettringite. Therefore, according to above-presented motivation, Fig. 2 is also evidence of the formation of ettringite. Hence, it may be concluded that the 6% $C_4A_3\bar{S}$ admixture content in aqueous solution under investigation was not sufficient to promote the fast precipitation of *isolated* ettringite particles with noticeable sizes during the specified observation time. Thus, it may be argued in a reliable way that the isolated crystals with hexagonal-prism shape observed in images presented in Fig. 1b–f do not belong to ettringite. However, because of chemistry of 6% $C_4A_3\bar{S}$ admixture-containing solution and its possible contamination with CO_2 it is necessary to consider also the possibility that these plate-like crystals are calcium monosulfate hydrate (AFm) and/or any polymorph of calcium carbonate ($CaCO_3$) since particles of these phases may also precipitate with a plate-like shape. Formation of $CaCO_3$ crystallites is expected due to through-solution precipitation according to the reaction $Ca^{2+} + CO_3^{2-} \rightarrow CaCO_3$. Therefore, for phase analysis of hydration products that form in 6% $C_4A_3\bar{S}$ admixture-containing solution, an XRD spectrum was recorded (see Fig. 3) from a sample prepared from this solution (for details of the sample preparation see the previous section). The spectrum presented in Fig. 3 indicates that the sample contains the raw unhydrated phases, i.e., the components of Portland cement and admixture: C_2S, C_3S, C_4AF, and $C_4A_3\bar{S}$ as well as hydration products: ettringite, C–S–H, and CH (the conventional notations in cement chemistry are used: C = CaO, A = Al_2O_3, S = SiO_2, $\bar{S} = SO_3$, and H = H_2O). From comparative analysis of the intensities of recorded diffraction peaks, it follows that the most part of the sample is composed of raw materials. This means that a 2-h period was not sufficient for the formation of hydration products in a large amount. The recorded XRD spectrum did not reveal the presence of AFm and $CaCO_3$ phases: either these phases did not form or their content is too small to be resolved. It is reliably established that, under sulfate reach condition, formation of the ettringite is preferable in comparison to AFm phase precipitation. Due to gypsum and $C_4A_3\bar{S}$ admixture content, our solution was rich by sulfate ions and their concentration is likely maintained on the high level during 2-h observation time (note that the XRD spectrum in Fig. 3 shows that, after 2-h period of hydration, the content of undissolved $C_4A_3\bar{S}$ admixture is still high). This facilitated preferential growth of the ettringite rather than formation of the AFm phase in accordance with results of XRD phase analysis (see Fig. 3). As to possible formation of the $CaCO_3$ phase, in analysis of the XRD spectrum, it was taken into account that calcium carbonate exhibits three main polymorphs: calcite, vaterite, and aragonite. Formation of the polymorphic form aragonite is stable at temperatures 40 °C [9]. Therefore, we may exclude the formation of the aragonite polymorph since our experiments have been conducted at much lower temperature, 25 °C. In aqueous solution, crystallites of calcite precipitate with different shapes depending on pH value [10], however, these shapes substantially differ from a distinct hexagonal-prism shape of particles identified in images in Fig. 1b–f as CH crystals. As to vaterite polymorph, in the aqueous solution the crystallites of vaterite precipitate with a spherulite-like form [11]. Interestingly, the crystal lattice parameters of vaterite are in such a relation with the CH lattice parameters that we may expect epitaxial growth of this polymorph on surfaces of the CH crystallites that precipitate in solution [10]. In an aqueous solution supersaturated with respect to CH, uncontrollable penetration of CO_2 into the solution leads to carbonation (presumably with vaterite) of the surfaces of growing CH crystallites rather than to precipitation of the calcium carbonate particles [12]. In turn, it is established on the basis of soft X-ray microscopy imaging [13, 14] that, as a rule, a noticeable carbonation of a cementitious solution is accompanied by appearance of chains or clusters of small air bubbles, which are potential suppliers of CO_2. In X-ray images presented in Figs. 1 and 2, there is no any evidence of the penetration of air bubbles into solutions; therefore, in our experiments a high degree of contamination with CO_2 and, hence, precipitation of the calcium carbonate crystals with noticeable sizes are improbable. Thus, from results of XRD phase analysis and above-presented arguments we may conclude in a reliable way that the crystallites with hexagonal-prism shape observed in X-ray images in Fig. 1 belong to CH.

As is clearly demonstrated in Fig. 1b–f, the relative locations and orientation of the growing CH crystals in solution are preserved in time. That is to say, during the growth process, no strong convective fluxes were generated in the solution and the growing particles remained immobile. Note in these figures that particle No. 1 is viewed along a ⟨*hki*0⟩ crystallographic direction, whereas particle

No. 2 is oriented in such a way that its {0001} basal facet (see also Fig. 4) is observed. Particle No. 1 is of special interest as it is viewed along a $\langle hki0 \rangle$ crystallographic direction (the {0001} facets of the particle exhibit a slight misorientation with respect to observation direction), and its stable orientation was favorable for simultaneous measurements of the linear sizes L_1 and L_2, depending on time and, hence, for evaluation of corresponding growth rates in both the $\langle 10\bar{1}0 \rangle$ and $\langle 0001 \rangle$ directions (see Fig. 4).

The limitations of the microscope (a resolution of 35 nm) does not allow observation of the nucleation process of the CH crystallites in solution from the very beginning of their formation. As a first approximation, however, it may be assumed that the nuclei of this phase possess a quasi-spherical shape and grow during the nucleation period, $0 < t < t_n$, with a constant rate, V_n, which defines the increase of the nucleus diameter, d, with time, according to a relationship [15]

$$d(t) = V_n t, \tag{2}$$

where

$$V_n = 2\Omega\beta_n(C - C_e), \tag{3}$$

t is the time, t_n is the duration of the nucleation period, Ω is the volume occupied by a molecule (unit cell) in a nucleus, β_n is the growth (nucleation) kinetic coefficient during the nucleation period, and C_e and C (in m^{-3} units) are the equilibrium concentration (solubility) and actual concentration of solute molecules, respectively. At time $t = t_n$, only a small part of the CH crystallites reaches a critical diameter (the size at which the stable growth of a particle is energetically more favorable) [15]:

$$d_n = \frac{4\,\Omega\,\gamma}{k\,T\,\ln S} \tag{4}$$

and continue to increase in size. A majority of the CH crystallites with sizes in the range $d < d_n$ does not reach the critical diameter because of a partial dissolution that results from thermal and supersaturation fluctuations. In Eq. 4, γ is the nucleus–water interfacial energy, T is the temperature, k is the Boltzmann constant, and S is the supersaturation ratio of the solution. Equation 2 yields an alternative expression for the critical diameter, $d_n = V_n t_n$, which is achieved at $t = t_n$. The following simple relationships connect parameters S, C_e, and C with the ionic product, K, and the solubility product, K_{sp}, of the CH:

$$S = \frac{K}{K_{sp}}, \quad C_e = \sqrt[3]{K_{sp}/4}, \quad C = \sqrt[3]{K/4}, \tag{5}$$

where, parameters $C_e \approx 7.83 \times 10^{24}\ \mathrm{m}^{-3}$ and $K_{sp} \approx 8.79 \times 10^{-6}\ \mathrm{M}^3$ are known [16].

During the post-nucleation period, where $t > t_n$, the CH nuclei that reach the critical diameter continue to grow through their preferential $\{10\bar{1}0\}$ and {0001} facets (see Fig. 4). For quantitative description of the growth process of CH particles at post-nucleation period, we may modify the theoretical results that are obtained for growth process of a spherical particle in a supersaturated solution. The growth rate of a spherical particle, $V = \partial d/\partial t$, in a saturated and non-mixing solution in isotropic approximation, is given by the following equation (see, e.g., [15, 17]):

$$\frac{\partial d}{\partial t} = \frac{2\Omega\beta(C - C_e)}{1 + \frac{\beta d}{2D}}, \tag{6}$$

where, d is the diameter of particle, $\partial d/\partial t$ is the derivative with respect to time, β is the isotropic growth kinetic coefficient that is assumed for a local surface area of the particle to be independent on crystallographic orientation, and D is the diffusion coefficient of solute particles; parameters Ω, C, and C_e were defined in Eq. 3. Note that in the limit of small sizes, $d \to 0$, Eq. 6 transforms into Eq. 3 once $\beta d/(2D) \ll 1$. Integrating Eq. 6 results in

$$d(t) = \sqrt{\left(\frac{2D}{\beta} + d_n\right)^2 + 8\Omega(C - C_e)D(t - t_n)} - \frac{2D}{\beta}, \tag{7}$$

where it is implied that parameter $d_n = d(t_n)$ is the value of diameter at the beginning $t = t_n$ of the post-nucleation period, $t > t_n$, and is defined by Eq. 4. According to our experimental observations (see Fig. 1b–f), the growing CH particles exhibit hexagonal-prism shape, and Eq. 7 is not valid for a realistic analysis of their shape evolution. To modify Eq. 7 for application to growth process of the CH, it is assumed that the growth kinetic coefficient, β, and the equilibrium concentration of solute molecules, C_e, differ at $\{10\bar{1}0\}$ and {0001} facets. This assumption is based on the following argumentation: The Curie-Wulff rule (see, e.g., [15]) is valid at a size scale $\lesssim 1$ μm of a precipitating particle and for equilibrium configuration of a CH crystallite can be expressed as follows:

$$\frac{L_1}{L_2} = \frac{\gamma_1}{\gamma_2}, \tag{8}$$

where, γ_1 and γ_2 are the interfacial energies between $\{10\bar{1}0\}$ and {0001} facets and solution, respectively; linear sizes L_1 and L_2 are defined in Eq. 1. The data extracted for linear sizes of particle No. 1 from images given in Fig. 1b–f give for the aspect ratio an estimate $r_L = L_1/L_2 \approx 2.7$, which in compliance with Eq. 8 predicts rather strong anisotropy for the surface energy of the CH. In addition, the estimate $L_1/L_2 \approx 2.7$ indicates that the growth rates of $\{10\bar{1}0\}$ and {0001} facets differ substantially. The difference in the growth rates of different types of crystallographic facets is caused by the two factors: anisotropy of the growth kinetic coefficient [15]; and dependence of the supersaturation ratio at the surface of a facet on its crystallographic type [18].

According to Eq. 5, the latter factor may be associated with individual solubility of a facet of a certain crystallographic type, i.e., with anisotropy of the solubility, C_e. At supersaturation conditions, the growth process of a particle in solution results from the two competitive processes, crystallization and dissolution, with the crystallization process dominating. Even at supersaturation conditions, detachment of a certain amount of adsorbed molecules (i.e., dissolution) takes place owing to local thermodynamic fluctuations of the supersaturation and temperature. At a given type of growth facet, the crystallization process (the transition of solute molecules from solution into an adsorptive layer and incorporation into crystallographic sites) is characterized by the growth kinetic coefficient, whereas the dissolution process may be quantified through individual solubility of the facet [18], i.e., through *local* concentration of solute molecules in solution at the facet. Generally, for a given facet, the near-facet concentration of solute molecules is associated with solubility of this facet. In the case under consideration here, there is no evidence to argue that for a given facet the near-facet concentration of solute molecules equals to solubility of this facet. In fact, it is more reasonable to assume that the higher solubility of the facet, the larger near-facet concentration of solute molecules in solution for this facet. Therefore, taking into account the above-presented estimate $\gamma_1/\gamma_2 \approx 2.7$ (see Eq. 8) for ratio of the surface energies of $\{10\bar{1}0\}$ and $\{0001\}$ facets, further analysis assumes that at these facets concentrations of solute molecules in solution differ. Accordingly, after replacements,

$$\beta \to \beta_i, \quad C_e \to C_{si}, \quad d \to L_i, \quad (i = 1, 2)$$

Equation 7 is now modified into the following set of expressions:

$$L_i(t) = \sqrt{\left(\frac{2D}{\beta_i} + d_n\right)^2 + 8\Omega(C - C_{si})D(t - t_n)} - \frac{2D}{\beta_i}, \quad (i = 1, 2) \tag{9}$$

where the subscript values $i = 1$ and 2 correspond to $\langle 10\bar{1}0\rangle$ and $\langle 0001\rangle$ growth directions (i.e., to $\{10\bar{1}0\}$ and $\{0001\}$ facets), respectively; L_i, β_i, and C_{si} are the linear size of the particle (see Eq. 1), kinetic coefficient and the concentration of solute molecules in solution at facets of the type i (i = 1, 2), respectively, and D is the diffusion coefficient of solute molecules. According to Eq. 9, at $t = t_n$,

$$L_1(t_n) = L_2(t_n) = d_n, \tag{10}$$

where now d_n is the initial value of the sizes L_1 and L_2 at the beginning of the post-nucleation period. Equation 10, a boundary condition that connects Eqs. 2, 4, and 9, expresses a continuous variation of the linear sizes of a growing particle at transition of the nucleation process into post-nucleation growth stage.

Equation 9 yields the growth rates in directions of interest, V_1 and V_2, as

$$V_i(t) = \frac{dL_i}{dt} = \frac{4\Omega(C - C_{si})D}{\sqrt{\left(\frac{2D}{\beta_i} + d_n\right)^2 + 8\Omega(C - C_{si})D(t - t_n)}}, \quad (i = 1, 2) \tag{11}$$

where, again, the subscript values $i = 1$ and $i = 2$ correspond to growth rates in directions $\langle 10\bar{1}0\rangle$ and $\langle 0001\rangle$, respectively.

Further analysis requires the numerical value of the nucleus–water interfacial energy, γ, introduced through Eq. 4. Unfortunately, the literature contains no data of this parameter for CH in aqueous solution. Brunauer et al. [4] determined experimentally the total surface energy of CH to be $\gamma_t = 1.18$ J/m^2, which may substantially differ from interfacial energy, γ, as these parameters differ in terms of the physical definition. The interfacial energy may be estimated from the following relationship [19]:

$$\gamma = \frac{qkT}{\Omega^{2/3}} \ln\left(\frac{1}{\Omega C_e}\right), \tag{12}$$

where q is the so-called shape parameter of a crystalline nucleus and accepts a value $q = 0.514$ if the shape of the nucleus is spherical. For data $\Omega = 5.488 \times 10^{-29}$ m^3, $C_e = 7.83 \times 10^{24}$ m^{-3}, $k = 1.38066 \times 10^{-23}$ J/K, $T =$ 298 K, and $q = 0.514$, a value $\gamma = 0.114$ J/m^2 is calculated using Eq. 12 for nucleus–water interfacial energy. Note that the obtained estimate $\gamma = 0.114$ J/m^2 for interfacial energy between CH and water by a factor of about 10 is smaller than the total surface energy of CH, $\gamma_t = 1.18$ J/m^2, reported by Brunauer et al. [4].

Figure 5 presents experimental data and corresponding theoretical curves for linear sizes d, L_1, and L_2 and for aspect ratio $r_L = L_1/L_2$ versus time for particle No. 1 (see Fig. 1b–f). For this particle, the experimental values of linear sizes L_1 and L_2 have been obtained through direct measurements of these parameters from recorded images (Fig. 1b–f). During the observation time-interval 31 min $< t <$ 118 min, the sizes L_1 and L_2 increased in the ranges 0.60 μm $< L_1 <$ 1.38 μm and 0.21 μm $< L_2 <$ 0.51 μm, respectively. The aspect ratio, $r_L = L_1/L_2$, calculated from experimental values L_1 and L_2, was practically stable during observation time, $r_L \approx 2.7$. In Fig. 5, the linear dependence $d(t)$ showed an increase of the nucleus size according to Eq. 2 at nucleation period, $t < t_n$, whereas the curves $L_1(t)$ and $L_2(t)$ represent the best fits to the experimental data at post-nucleation period, $t > t_n$, according to Eq. 9. The dependencies $L_1(t)$ and $L_2(t)$ were achieved in the following way. First, applying the method of polynomials least-squares fitting, we found

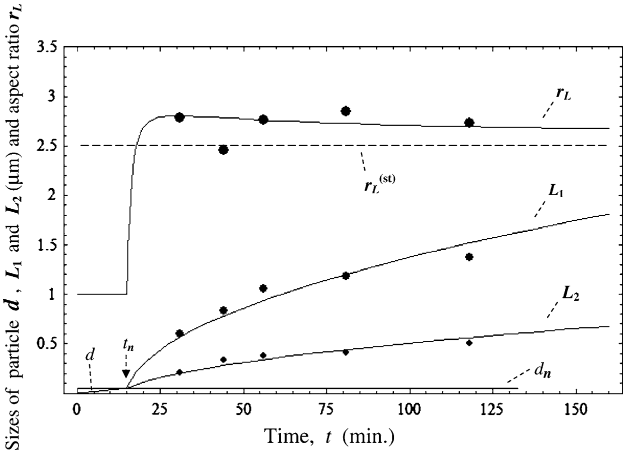

Fig. 5 Variation of the linear sizes d, L_1 and L_2 of particle 1 depending on time. At nucleation period, $0 < t < t_n$, the particle size d increases linearly according to Eq. 2 (solid inclined line). The horizontal solid line corresponds to nucleation critical diameter $d_n = 0.05$ μm. At post-nucleation period, $t > t_n$, the medium and small size dots and curves $L_1(t)$ and $L_2(t)$ represent experimental data and the best fits according to Eq. 9 for sizes L_1 and L_2, respectively; large dots and curve $r_L(t) = L_1(t)/L_2(t)$ represents experimental data and the theoretical curve of the aspect ratio over period $t > 0$. In compliance with boundary condition 10, $d(t_n) \equiv d_n = L_1(t_n) = L_2(t_n)$. At $t > 25$ min, the aspect ratio is maintained at a maximal level $r_L \approx 2.7$. The horizontal dashed line corresponds to asymptotic limit $r_L^{(st)} = 2.5$ at $t = \infty$ according to Eq. 13

interpolation curves $L_1^{(in)}(t)$ and $L_2^{(in)}(t)$ for experimental L_1 and L_2 data, respectively. The intersection point of curves $L_1^{(in)}(t)$ and $L_2^{(in)}(t)$ yielded the duration of the nucleation period and critical diameter of nucleus, $t_n \approx 15$ min and $d_n \approx 0.05$ μm (see Fig. 5). Next, using the data $\Omega = 5.488 \times 10^{-29}\text{m}^3$, $k = 1.38066 \times 10^{-23}$ J/K, $T = 298$ K, $\gamma = 0.114\,\text{J/m}^2$, $C_e = 7.83 \times 10^{24}\ \text{m}^{-3}$, and $K_{sp} \approx 8.79 \times 10^{-6}$ M [16], from the set of Eqs. 4 and 5 the value of the actual concentration of solute molecules was calculated to be $C = 8.22 \times 10^{24}\ \text{m}^{-3}$. Thus, for each dependence, $L_i(t)$ ($i = 1, 2$), given by Eq. 9, the number of unknown parameters is reduced to three: β_i, D, and C_{si}. Finally, using Eq. 9, the best fits of dependencies $L_1(t)$ and $L_2(t)$ to experimental data were achieved at values of unknown parameters $\beta_1 = 6254$ μm/min, $\beta_2 = 5920$ μm/min, $D = 222$ μm²/min, $C_{s1} = 7.970 \times 10^{24}\ \text{m}^{-3}$, and $C_{s2} = 8.181 \times 10^{24}\ \text{m}^{-3}$. Note that curves $L_i^{(in)}(t)$ and $L_i(t)$ ($i = 1, 2$) practically coincide therefore, Fig. 5 only presents the latter curves.

Using Eqs. 2–5, the following data was calculated for the next group of unknown parameters: $K = 10.18 \times 10^{-6}\ \text{M}^3$, $S = 1.158$, $V_n = 0.003$ μm/min, and $\beta_n = 78$ μm/min. Then, using Eq. 11, the average growth rates in directions $\langle 10\bar{1}0\rangle$ and $\langle 0001\rangle$ during the post-nucleation period were determined to be $\overline{V_1} = 0.014$ μm/min and $\overline{V_2} = 0.005$ μm/min, respectively.

In spite of a large number of fitting parameters, β_1, β_2, D, C_{s1}, and C_{s2}, the best fits for curves $L_1(t)$ and $L_2(t)$ to the experimental data were easily obtained using Eq. 9 (see Fig. 5), because Eq. 9 exhibits considerably different parametric dependencies on kinetic and diffusion coefficients. According to Eq. 9, at the beginning of the post-nucleation period, $t_n \approx 15\ \text{min} < t \lesssim 20$ min (see Fig. 4), the size variation is controlled by the surface kinetic processes. Therefore, the main fitting parameters are the kinetic coefficients β_1 and β_2. At a later stage, $t \gtrsim 20$ min, it follows that the growth process is driven predominantly by the diffusion, and, accordingly, the main fitting parameter is the diffusion coefficient, D.

Interestingly, for an infinitely large observation time, Eq. 9 yields for the aspect ratio the following limit:

$$r_L^{(st)} = \operatorname*{Lim}_{t\to\infty}[L_1(t)/L_2(t)] = \sqrt{\frac{C - C_{s1}}{C - C_{s2}}} \tag{13}$$

At determined values $C = 8.22 \times 10^{24}\ \text{m}^{-3}$, $C_{s1} = 7.970 \times 10^{24}\,\text{m}^{-3}$, and $C_{s2} = 8.181 \times 10^{24}\,\text{m}^{-3}$, Eq. 13 yields for our case a limit $r_L^{(st)} \approx 2.5$. In turn, Eq. 13 leads to another important limit:

$$\operatorname*{Lim}_{C\to\infty} r_L^{(st)} = 1, \tag{14}$$

which predicts that at large concentration of solute molecules the shape of a growing particle is expected to be geometrically more homogeneous in different crystallographic directions. A numerical analysis of Eq. 13 shows that: (i) parameter $r_L^{(st)}$ rapidly increases once the actual concentration of solute, C, approaches its near-surface concentration at $\{0001\}$ facets, $C_{s2} = 8.181 \times 10^{24}\,\text{m}^{-3}$; and (ii) a value $r_L^{(st)} = 1$ evaluated according to Eq. 14 is the lower limit of the aspect ratio.

Discussion and main conclusions

Precipitating CH crystallites were observed in images recorded from other volumetric regions of the solution. Using statistics, the values of the same parameters characterizing the growth process were extracted in the same way detailed above from analysis of images of three other CH particles. For each physical parameter, the data extracted from analysis of images of four CH particles exhibit dispersion of no more than 5% (for the sake of brevity, these additional images and corresponding data evaluated for growth parameters from these images is not presented). Therefore, all the physical parameters evaluated from analysis of the precipitation of particle No. 1 may be considered to be characteristic for the growth process of the CH phase in solution under investigation. According to plots presented in Fig. 5 for particle No. 1, the growth process of the CH crystals in solution may be quantitatively described as follows: At nucleation period with a duration of $t_n \approx 15$ min, the CH quasi-spherical nuclei grow in size at growth rates of about of $V_n = 0.003$ μm/min. At the end of this nucleation period, only a small amount of these nuclei achieve the critical size $d_n \approx 0.05$ μm and continue to increase in size during the post-nucleation period, $t > t_n$. At an initial stage of the post-nucleation period, 15 min $< t <$ 25 min, the aspect ratio of the particles rapidly increases from $r_L(t_n) = 1$ to a maximal value $r_L^{(\max)} \approx 2.7$, which is more or less maintained during the succeeding time-interval of the observation time, 25 min $< t <$ 118 min . Such behavior of the aspect ratio is presumably caused by a rapid transformation of quasi-spherical shape of the nuclei into a polyhedral crystalline shape, and further transformation of the polyhedral shape into a stable hexagonal-prism shape (see Fig. 4). The former shape transformation may be associated with formation, except of $\{10\bar{1}0\}$ and $\{0001\}$ facets of the CH, also of other type small-index crystallographic facets, such as $\{1\bar{2}10\}, \{10\bar{1}1\}$, and $\{10\bar{1}2\}$. The latter shape transformation results from gradual vanishing of all the type crystallographic facets, except in the case of the $\{10\bar{1}0\}$ and $\{0001\}$ facets. The CH crystals grow at post-nucleation period of 15 min $< t <$ 118 min through their preferential $\{10\bar{1}0\}$ and $\{0001\}$ facets, with the average growth rates $\overline{V_1} = 0.014$ μm/min and $\overline{V_2} = 0.005$ μm/min, respectively. Note that during the growth process, it is presumed that facets like $\{1\bar{2}10\}, \{10\bar{1}1\}$, and $\{10\bar{1}2\}$ form and then vanish, since their surface energies and, hence, the growth rates exceed the same parameters associated with $\{10\bar{1}0\}$ and $\{0001\}$ facets [20]. As predicted by theoretical dependence $r_L(t)$ for the post-observation time $t > 118$ min (see Fig. 5 and Eq. 13), the aspect ratio tends to a stationary value, $r_L^{(st)} \approx 2.5$ provided that evaluated values of concentrations C, C_{s1}, and C_{s2} are maintained constant in time. Future analysis [21] will examine whether concentrations C_{s1} and C_{s2} introduced in Eq. 9 may be associated with dissolution rates and individual solubility of $\{10\bar{1}0\}$ and $\{0001\}$ facets, respectively.

From Eqs. 13 and 14, it may be assumed that through manipulation of the actual concentration of dissolved stoichiometric molecules, C, it is possible to control the aspect ratio of precipitating particles of CH crystals. This has implications from the technological standpoint in the production of cementitious materials, because the aspect ratio of a crystal with known shape and type of crystallographic facets facilitates quantitative estimates of a cement's adhesive ability at different environmental and physical conditions. A lower limit $r_L^{(st)} = 1$ evaluated in this work for the aspect ratio of precipitating CH crystals in aqueous solution is in agreement with values obtained by other researchers [4–7] (see the relationship given by Eq. 1).

This study demonstrated that the synchrotron radiation transmission microscopy may serve as an effective tool not only for observation of the hydration of cementitious particles in aqueous solutions [2], but also is a valuable technique for *quantitative analysis* of the through-solution precipitation process of different stoichiometric phases of the cement paste. Experimental results based on the proposed theoretical model enabled evaluation of the main physical parameters that characterizes the growth process of the CH crystals: supersaturation ratio, kinetic and diffusion coefficients, nucleation critical size, crystal aspect ratio, and growth rates for different crystallographic facets. A theoretical justification is presented for the lower limit that exhibits the aspect ratio of the CH crystals in cementitious solutions and hardened cement pastes.

Acknowledgements Authors would like to express their gratitude to Dr. D.A. Silva and Dr. K. Benzarti for valuable discussions. The research described in this publication was made possible in part by Award No. ARP2-2610-YE-04 of the U.S. Civilian Research and Development Foundation for the Independent States of the Former Soviet Union (CRDF). The operations of the ALS are supported by the Director, Office of Science, Office of Basic Energy Sciences, Materials Sciences and Engineering Division, of the U.S. Department of Energy under Contract No. DE-AC02-05-CH11231.

References

1. Gartner EM, Kurtis KE, Monteiro PJM (2000) Cement Concrete Res 30:817
2. Juenger MCG, Lamour VHR, Monteiro PJM, Gartner EM, Denbeaux GP (2003) J Mater Sci Lett 22:1335
3. Kurtis KE, Monteiro PJM, Brown JT, Meyer-Ilse W (1998) Cement Concrete Res 28:411
4. Brunauer S, Kantro DL, Weise CH (1956) Can J Chem 34:729
5. Rodriguez-Navarro C, Hansen E, Ginell WS (1998) J Am Ceram Soc 81:3032
6. Boyer JP, Berger RL (1980) J Am Ceram Soc 63:575
7. Teramoto H, Koie S (1976) J Am Ceram Soc 59:522
8. Mehta PK (1973) Cement Concrete Res 3:1
9. Sawada K (1997) Pure Appl Chem 69:921
10. McCaulay JW, Roy R (1974) Am Mineral 59:947
11. Kralj D, Brecevic L, Nielsen AE (1990) J Cryst Growth 104:793
12. Perruchot C, Chehimi MM, Vaulay MJ, Benzarti K (2006) Cement Concrete Res 36:305
13. Juenger MCG, Monteiro PJM, Gartner EM, Denbeaux GP (2005) Cement Concrete Res 35:19
14. Kirchheim AP, Monteiro PJM, Fisher P, Dal Molin DC Cement Concrete Res (to be published)
15. Vainshtain BK (1980) Modern crystallography vol 3: Formation of crystals. Nauka, Moskow
16. Gartner EM, Tang FJ, Weiss SJ (1985) J Am Ceram Soc 68:667
17. Parker RL (1970) Crystal growth mechanisms: energetics, kinetics and transport, solid state physics, vol 25. Academic Press, New York and London
18. Khamskii AV (1967) Crystallization in solutions. Nauka, Leningrad, p 49
19. Kashchiev D, van Rosmalen GM (2003) Cryst Res Technol 38:555
20. Laudise RA (1970) The growth of single crystals. Prentice-Hall, New Jersy
21. Harutyunyan VS, Kirchheim AP, Monteiro PJM, Aivazyan AP, Fischer P J Am Ceram Soc (to be published)